

Supplementary Materials for

Quantitative Imaging of Epithelial Cell Scattering Identifies Specific Inhibitors of Cell Motility and Cell-Cell Dissociation

Dinah Loerke, Quint le Duc, Iris Blonk, Andre Kerstens, Emma Spanjaard, Matthias Machacek, Gaudenz Danuser,* Johan de Rooij*

*To whom correspondence should be addressed. E-mail: j.derooij@hubrecht.eu (J.d.R.); Gaudenz_Danuser@hms.harvard.edu (G.D.)

Published 3 July 2012, *Sci. Signal.* **5**, rs5 (2012)
DOI: 10.1126/scisignal.2002677

This PDF file includes:

Note S1. Phase-contrast image analysis, cell detection, and tracking.
Note S2. Quantifying cell migration and dealing with mitotic cells.
Note S3. Quantifying spatial dispersal using Ripley's K function.
Note S4. Quantifying cell-cell adhesion.
Note S5. Hierarchical clustering.
Fig. S1. Cell tracking.
Fig. S2. Definition of spatial dispersion parameter based on Ripley's K function.
Fig. S3. Definition of adhesion loss parameter based on motion correlation.
Fig. S4. Inhibition efficiency for motility, dispersal, and adhesion loss parameters.
Fig. S5. Ranked inhibition efficiencies.
Fig. S6. Validation of hierarchical clustering.
Fig. S7. Velocity differences indicate adhesion specificity.
Fig. S8. Inhibition efficiency of effective drugs on the scattering of normal and cell-cell junction-compromised MDCK cells.
Table S1. Target names and additional information on drugs used in screen.
References
Legends for Movies S1 to S8

Other Supplementary Material for this manuscript includes the following: (available at www.sciencesignaling.org/cgi/content/full/5/231/rs5/DC1)

Movie S1 (.mp4 format). The presence of cell-cell adhesions slows down HGF-induced cell motility.
Movie S2 (.mov format). Motility parameter.
Movie S3 (.mov format). Spatial dispersion parameter.

Movie S4 (.mov format). Adhesion loss parameter.

Movie S5 (.mp4 format). α -Catenin-depleted cells do not form functional cell-cell junctions.

Movie S6 (.mp4 format). Knockdown of CDK1 but not CDK5 inhibits the HGF-induced increase in cell motility.

Movie S7 (.mp4 format). Diclofenac inhibits the HGF-induced loss of cell-cell adhesion, whereas knockdown of COX-2 reduces the stability of cell-cell junctions.

Movie S8 (.mp4 format). Blocking RSKs by chemical inhibition or siRNA-mediated knockdown inhibits the HGF-induced increase in cell motility.

Note S1: Phase-contrast image analysis, cell detection, and tracking.

The ScatterTrack image-analysis software was developed to automatically process large data sets with minimal requirements for user interaction. The image processing consists of

- image segmentation to detect cell locations and clusters, based on adaptive intensity threshold selection in the intensity distribution of the raw images for the distinction of cell nucleus, cell area, and cell-free image background;
- cell tracking, using a global nearest neighbor method to resolve possible assignment conflicts between source and target points (1).

After cells were detected in a frame, their positions were associated by the global nearest neighbor method to the cell positions in the previous frame. The procedure yields a list of cells without correspondence in the previous frame (referred to as “new” cells), and a list of cell positions in the previous frame that could not be assigned to any of the available positions in the current frame (referred to as lost cells). New and lost cells are subsequently processed in a gap closing step, aimed at linking broken trajectories due to temporary detection errors. Thus, gap closing maximizes the length of the detected trajectories, while the detection step maximizes the number of cells. Both strategies are critical to the system’s ability to accommodate cell division.

A flow-chart of the algorithm is shown in Fig. S1A. First, the overall intensity variance of the image was tested to determine whether the frame contained discernible objects. If the variance was close to 0, the segmentation algorithm will not find any objects in the image; this situation could occur due to shutter malfunction, overexposure, temporary defocus, or lack of cells present in the field of view. The frame was rejected and stored in a “bad frame” list. If the intensity variance as sufficient for segmentation, the image was corrected for shading in the background, a phenomenon typical for low magnification phase contrast images. After background correction, the image was segmented into three features associated with three intensities: dark nuclei, white halos, and grey background. The intensity thresholds were determined by k-means clustering (2) (Fig. S1B). Subsequently, cell coordinates were calculated as the centroids of the nuclei (red dots in Fig. S1B, panel II).

Second, cells were tracked by linking cell coordinates found in the current frame to the track heads of the growing tracks in the previous frame using the global nearest neighbor approach as

discussed (1). Using the lists of ‘lost’ and ‘new’ cells, gaps were closed if unassigned track heads existed within the past 5 frames that fell inside a search radius derived from the time gap to be closed and the typical cell speed. Detected halos were also stored and used to fill these gaps. This rescued tracking of cells lost in detection due to short periods of rounding which obscures the dark nuclear area. Cell coordinates in the gap were linearly interpolated. The last step was assigning cell properties, such as the number of cells in each segmented island, which defined if a cell was isolated or part of a cell cluster. Third, a pruning step restricted valid cell trajectories to those which were tracked for at least two consecutive frames.

To evaluate the efficiency of the automated detection algorithm, the results were compared to manual detection in one representative time lapse movie (the same used for movies S2 to S4). The fidelity of the automated detection was 90-95% before stimulation (Fig. S1C). Upon HGF stimulation, the fidelity first increased slightly during the cell spreading phase when nuclei were better separated from each other, and subsequently, as cells change morphology and detach from each other, it decayed to 80-85%. One explanation for inaccuracies in detection is the rounding of mitotic cells, which obscures their phase-dense nuclei. In resting MDCK cells, ~ 4% of the cells are in mitosis; this fraction increases to ~6% upon HGF treatment (see below). In DU-145 cells, division rates are lower.

To ensure that the three scattering parameters (described in more detail in notes S2 and S3) were not affected by a 10% reduction of the detection efficiency upon stimulation, we performed a ‘jackknife’ error estimation. In 100 iterations, 10% of the trajectories occurring 4 hours after stimulation were randomly deleted before parameter calculation. We found that this deletion caused only a slight underestimation of the normalized parameters, by 0.038 ± 0.011 at the reference timepoint 12 hours after stimulation. Thus, we conclude that the loss in detection efficiency during the progression of scattering does not affect the accuracy of the parameters.

For examples of tracking results from time lapse image series under different experimental conditions, see movie S1. Dragtails visualize the automatically determined cell positions in the last 6 frames.

Note S2: Quantifying cell migration and dealing with mitotic cells.

I. Quantifying cell migration.

The image segmentation and subsequent cell-centroid tracking yielded trajectories that were then processed to extract the three parameters quantifying the cell scattering behavior. We used a sampling rate of 10 min per frame, and our measured migration velocity is defined as the absolute displacement of cells in 20 min. This definition is based on 2 considerations:

- 1) Sampling rate: accuracy of tracking compared to technical limitations.

The sampling rate affects the accuracy of tracking when cellular displacements from frame to frame get close to half the mean distance between cells (3). In general, higher sampling rates will allow more accurate tracking; however, for practical reasons the sampling rate is limited to 10 min/frame in the multi-well microscopy setup used in our screening assay. The fastest population of MDCK cells after prolonged HGF treatment migrated at a velocity of 3 $\mu\text{m}/\text{min}$ (see Figs. 2B and 3C). Within 10 minutes these cells have thus traveled about 30% of their minimal intercellular distance (MDCK cells have an average diameter of 100 μm). Therefore global nearest neighbor based tracking was still sufficient at this sampling rate even for fast-moving cells. We tested faster sampling rates (down to 1 min per frame) and did not observe differences in the migration velocities measured from the resulting tracks.

Migration velocity: persistent compared to instantaneous movement

Measuring the velocity in a short time window (for example, frame-to-frame) makes it possible to capture the instantaneous velocity and migration behavior of the cell, which may include random small-scale movement of the cell. However, frame-to-frame measurements are also inherently more sensitive to - and may be inflated by - noise in the measured cell positions. In contrast, velocities measured over longer time windows (for example, based on the net displacement over 10 frames) tend to 'smooth out' random frame-to-frame displacements, both those caused by positional noise and those that represent real undirected motion. Thus, measurements over larger time windows better describe the cells' ability to sustain motion into a specific direction over extended periods and distances (directional persistence). In this study, the choice of motility measurement over 20 min allowed some reduction of positional noise while still capturing instantaneous turns of cells. Our rationale was that even instantaneous motion with low directional persistence would be an important indicator of the migratory competence of cells. Although the motility parameter thus has low sensitivity to directional persistence of motion (or lack thereof), the effects of motion persistence were reflected in the spatial dispersal parameter, where - for a

given increase in the migration speed - more persistent motion will allow a population of cells to disperse faster.

An alternative approach to separate the effects of changes in instantaneous motion speed and directional persistence would be to fit trajectories with the persistent random walk model (4, 5). However, these models rely on the assumption that the trajectory is governed by stationary parameters over the duration of the time window. Moreover, stable fits require windows of 20 and more time points. Given the transient behavior of cells after HGF stimulation, we cannot assume that the trajectories fulfill the conditions of stationarity over long enough time windows. Therefore, the simpler approach of computing the velocity of cells over a time window of 3 time points is more appropriate in this case.

II. Dealing with mitotic cells

Cells in mitosis round up and temporarily stop migrating; thus, to prevent dividing cells from lowering the measured velocity, they should ideally be systematically excluded from velocity measurements. Our assay ignored most cells that were rounded for prolonged periods of time because they temporarily 'disappear' from detection (see above), but it did not systematically identify and subsequently discard all dividing cells; thus, in principle, stimulations and perturbations that increase the percentage of cells in mitosis (for example, those that block progression through mitosis or increase in cell division rates) could affect the cell velocity measurement. It should be noted however, that even in HGF stimulated conditions, MDCK cells divide once every 12 hours (DU145 cells once every 18 hours), and mitosis lasts about 40 min. Thus, the percentage of cells in mitosis at any given time point after HGF stimulation does not exceed 6%. This small percentage, together with the reduced detection probability of rounded cells, indicates that effects on mitosis are not likely to affect the motility parameter in our assay. Moreover, drugs that increase cell division rate are rare, and existing drugs that block cells in mitosis (like nocodazole and other microtubule drugs) cause all cells to round up, which is easily recognized from the tracking results because of the decrease in cell numbers. The software would thus detect those incidences and the associated agents should be further analyzed for mitosis defects and toxicity. As an example and verification of these considerations, we have performed extended analyses, using the output from the tracking algorithm to verify the migration specific effect of depletion of the cell cycle kinase CDK1 in Fig. 7A.

Note S3: Quantifying spatial dispersal using Ripley's K function

I. Ripley's K-function

The quantitative description of cells' spatial dispersal in this study is based on Ripley's K-function (6). The K-function is widely used as a statistical descriptor of spatial clustering in ecology and astronomy, and has recently been applied to microscopy data (7), for example to study the distribution of specific cell types in tissue (8), or the distribution of specific subcellular structures (9-14).

Ripley's K-function $K(r) = N_r / \pi \rho$ specifies how many neighbors N are found within a certain distance r of a given cell, averaged over all cells in the image and normalized by the total cell density ρ (see the example in Fig. S2, A and B). In a completely random spatial distribution, the average number of neighbors depended only on the search area and the cell density as $N_r = \rho \cdot \pi r^2$, hence $K(r) = r^2$ (dashed line in Fig. S2B). Deviations in the measured $K(r)$ function from the r^2 -parabola reflected deviations of the cell locations from spatial randomness: Significantly higher values indicated more neighbors for a cell than expected for spatial randomness (clustering); significantly lower values indicated less neighbors than expected for spatial randomness (exclusion). To visualize deviations from r^2 , it was convenient to use a linearized version of the K-function, such as the L-function $L(r) = \sqrt{K(r)} - r$ (panel insert in Fig. S2B). In the L-function, a spatially random distribution corresponds to zero, so that positive values (here at distances 50-250 pixels) reflected cell clustering in islands, whereas negative values (here at distances 250-450 pixels) reflected exclusion (the 'empty' space between clusters).

II. Boundary Correction

Determining the K-function for objects near the border of the image poses the problem that not all of these cells' actual neighbors are visible in the field of view. Various boundary correction methods have been proposed in the literature to account for this effect. In this assay, we used Ripley's correction, which weighs the number of visible neighbors in the circle of radius r by a correction factor corresponding to the fraction of the circle's circumference that falls inside the field of view. In an image of size (l_x, l_y) and for an object with distance (x, y) from the nearest edge, this correction factor can be derived from simple geometrical considerations (15) as:

$$c(x, y, r) = \begin{cases} \frac{\pi/2 + \sin^{-1}(y/r) + \sin^{-1}(x/r)}{2\pi} & \text{if } r > \sqrt{x^2 + y^2} \\ \frac{2\sin^{-1}(y/r) + 2\sin^{-1}(x/r)}{2\pi} & \text{if } \sqrt{x^2 + y^2} \geq r > \max(x, y) \\ \frac{\pi + 2\sin^{-1}(\min(x, y)/r)}{2\pi} & \text{if } \max(x, y) \geq r > \min(x, y) \\ 1 & \text{elsewhere} \end{cases}$$

This formula is valid for distances up to $r_{\max} = \min(|x|, |y|)/2$, for which the circle of radius r extends over no more than two of the image borders.

III. Dispersal parameter from Ripley's K-function

The L-function $L(r, t)$ was calculated for every frame of the movie. In stimulated cells, the measured function flattened out as the cells disperse (Fig. S2C). To capture the time course of spatial dispersal in a single parameter $p_{disp}(t)$, we extracted the partial integral of the $L(r, t)$ function

$$p_{disp}(t) = \int_{d_1}^{d_2} L(r, t) dr$$

between the distances d_1 and d_2 . These distances were determined from the function $L(r, t_0)$ recorded prior to stimulation and then were kept fixed; d_1 represented the distance where $L(r, t_0)$ crosses from negative to positive values (approximating the average cell diameter), and d_2 was the position of the first maximum of $L(r, t_0)$ (approximating the average cluster diameter).

To ensure that this parameter responded to scattering as expected, we performed simulations (Fig. S2D): When a distribution of clustered points was allowed to move, but was kept together by attractive forces, the parameter did not change. When the attraction was removed and the points gradually dispersed in space by diffusion, the parameter decayed. When in addition the speed was increased, the decay became faster.

In cell measurements, the dispersal parameter is normalized with respect to the value prior to stimulation and to the end value measured in an HGF-only experiment. Therefore, the normalized parameter ranges between 0 and 1. Movie S3 shows an example of cell scattering, the associated flattening of the L-function, and the corresponding increase of the normalized spatial dispersal parameter over time.

IV. Growth Correction

The dispersal parameter is affected by cell division. Although the L-function is invariant with respect to cell density, new cells appearing over the course of the movie are not added in random positions; rather, cell division result in systematic growth of existing clusters, which ‘stretches’ the L-function in x-direction over time and causes a systematic distortion of the dispersal parameter.

To account for this effect, every measurement of the dispersal parameter in a frame was accompanied by a simulation of cluster growth (Fig. S2E). The cell distribution prior to HGF-stimulation defined the mean nearest-neighbor distance (NDD) probability function under clustered conditions. Throughout the movie, cell division was simulated by randomly adding new points to the edge of existing clusters, at positions allowed by the NDD distribution. The number of points added per frame was equal to the increase of cell positions detected in between two frames of the movie. Three separate simulations of cell division were performed per frame. The average difference between the L-functions and dispersal parameters with and without cell division indicated the distortion of these measures due to cell division. The distortion values were subtracted from the experimentally observed dispersal parameter to yield the growth-corrected parameter used for final analysis. The growth-corrected dispersal parameter of unstimulated cells (which divide but do not scatter) was constant over time (Fig. 2H), indicating the functionality of this growth-correction.

Note S4: Quantifying cell-cell adhesion

Cells attached to their neighbors tend to move together, whereas dissociated cells move independently from each other. This can be quantified through the motion correlation of neighboring cells, as defined by the cosine of the angle between the displacement vectors:

$$corr = \cos \alpha = \frac{u \cdot v}{|u| \cdot |v|} = \frac{(u_1 v_1 + u_2 v_2)}{\sqrt{(u_1^2 + u_2^2)} \cdot \sqrt{(v_1^2 + v_2^2)}}$$

where $u = (u_1, u_2)$ and $v = (v_1, v_2)$ are the displacement vectors of two neighboring cells from frame n to frame $n+s$, and the resulting correlation (*corr*) is a dimensionless number between -1 and 1. For uncorrelated motion, the average correlation value – averaged over all available point pairs in a population – is zero. For correlated motion, the average correlation value is positive.

Due to the pairwise analysis and statistical nature of the correlation measurement, averaging over a population was required. However, to relate the velocity of an individual cell to the adhesion status of the same cell, as measured by motion correlation, a correlation value had to be estimated for each cell. For this purpose, the correlation scores between the target cell and all its neighbors within the distance d_2 (see Note S2, section III) were averaged. If less than 3 neighbors fulfilled the distance criterion, the next neighbors were added until three correlation values per frame were available for averaging. In addition, the motion correlation with each neighbor was averaged over 5 consecutive frames to provide sufficient statistics for each individual cell and to capture correlation on various time scales. In assays with low positional noise, this time window can be reduced if higher time resolution is desired.

Before stimulation with HGF, the histogram of correlation values is skewed to positive values (Fig. S3A). 12 hours after stimulation, the mean motion correlation is shifted towards zero and the distribution is symmetric (Fig. S3B). To monitor the change of the histogram over time, the correlation histogram was fitted at each time point with the superposition of two distributions: A distribution of ‘detached’ cells represented by a zero-mean Gaussian, and a distribution of ‘attached’ cells represented by a positive-mean skewed Weibull function (see dashed magenta lines in Fig. S3, A and B). This superposition was motivated by the fact that (i) attached cells with a non-zero migration velocity have to display positive net motion correlation values (this requirement is physically necessary for cells in order to stay within each other's vicinity), so that attached cells are expected to give rise to a positive mean correlation 'mode'; (ii) detached cells that lack physical coordination with their neighbors (other than exclusion) are expected to display zero net correlation values, giving rise to a zero mean correlation 'mode'; (iii) attached and detached cells generally co-exist in these movies. Even in unstimulated conditions, there is usually a small subpopulation of single cells not attached to any cluster; in stimulated cells, individual cells

transform and detach (contributing to the zero-mean mode) whereas some clusters of attached cells remain stable for continued periods of time (contributing to the positive-mean mode).

In HGF-stimulated cells, the relative weight ratio of the two distributions (attached or detached) decays from typically ~ 0.9 prior to stimulation to ~ 0.1 at 12 hours following stimulation. Movie S4 shows an example of cell scattering, the gradual shift of the correlation histogram, and the corresponding increase of the normalized adhesion loss parameter over time.

Note S5: Hierarchical clustering

An inhibitor's efficiency was defined as one minus the ratio of the normalized parameter values of the drug-treated condition ('HGF+drug') compared to that of the reference sample ('HGF'), yielding an efficiency value ranging between 0 (0%, lowest efficiency, or no inhibition) and 1 (100%, highest efficiency, or complete inhibition) (Fig. S4). For each parameter (motility, adhesion, dispersal), a separate single value for the efficiency was extracted at 12 hours post-stimulation, so that each drug condition - drug X at concentration Y - was characterized by a triplet of efficiency values: efficiency in inhibiting adhesion loss, efficiency in inhibiting motility increase, and efficiency in inhibiting spatial dispersal.

After ranking drugs ranked based on their maximum efficiency (Fig. S5), we chose the 39 most efficient drug conditions - those that exceeded 66% (0.66) efficiency for at least one of the three parameters - for hierarchical clustering. We performed hierarchical clustering with single linkage as linkage method, which requires the definition of a metric or a semi-metric that defines the dissimilarity of data points. We used the Euclidian distance in the three-dimensional parameter space defined by the three inhibition frequencies.

The hierarchical clustering by itself does not provide a measure of the significance and the robustness of groups. Therefore, we performed a validation of the clustering results following previously described strategies (16).

As a first exploratory step, we visualized the clustering results in the 3D feature space (Fig. S6A). The data fall into three distinct groups with little to no significant overlap, in that the spread of

points within the cluster is small compared to the distance between neighboring clusters. Indeed, we find that the separation, or the mean distance between cluster centers (16), amounts to 0.60, whereas the compactness, or the mean distance of data points from their corresponding cluster center (16), amounts to 0.22. Next, we confirmed that the assignment of the individual data points to the three clusters is identical when the clustering is performed by k-means clustering instead of hierarchical clustering.

To quantitatively assess the quality of the clustering, we used the Dunn index as an internal measure (17). The Dunn index relates the minimum distance of points in one cluster from points in the nearest neighboring cluster to the maximum distance between points within the same cluster; a higher Dunn index value indicates better cluster separation, or a better quality of the partitioning. First, we confirmed that the selection of 3 clusters resulted in the best partition of the complete dataset. To accomplish this, we forcibly partitioned the data into 2-9 clusters and calculated the Dunn index for each solution (Fig. S6B). The Dunn index has a clear maximum at 3 clusters, indicating that with 2 clusters the data is under-partitioned and with 4 and more clusters the data is over-partitioned. Second, we performed simulations in which we took the full dataset, but assigned each data point randomly to one of the three clusters, and re-calculated the Dunn index for the new assignments. For 500 simulations, the Dunn index was an order of magnitude below that of the cluster assignment presented in Fig. 5A, underlining the high statistical significance of this result.

To test the robustness of the clusters, we established 'self-consistency' by drawing overlapping sub-samples of the complete data set (corresponding to randomly deleting 10% of the points), re-clustering with hierarchical clustering, and determining the center-of-mass of the updated clusters (Fig. S6D). In particular, this procedure would reveal adverse influences of data outliers. The deviation of the sub-sampled data sets from the full data sets was 0.0845 for the non-specific cluster, and 0.0432 and 0.0469 for the motility- and adhesion-specific clusters, respectively. It should be noted that this scatter is 3 to 5 times less than the compactness of the individual clusters, although the cluster of unspecific efficient inhibitors is somewhat unstable. This is mainly associated with the fairly low number of data points, where elimination of 2 to 3 individual points from the cluster may cause substantial shifts of the cluster centers. Nonetheless, even with the worst case scenario, the three clusters remain well separated. Together, these tests indicated that

the partitioning by hierarchical clustering of efficient inhibitors of cell scattering into 3 classes – ‘adhesion-specific’, ‘motility-specific’, and ‘unspecific’ – is valid and robust.

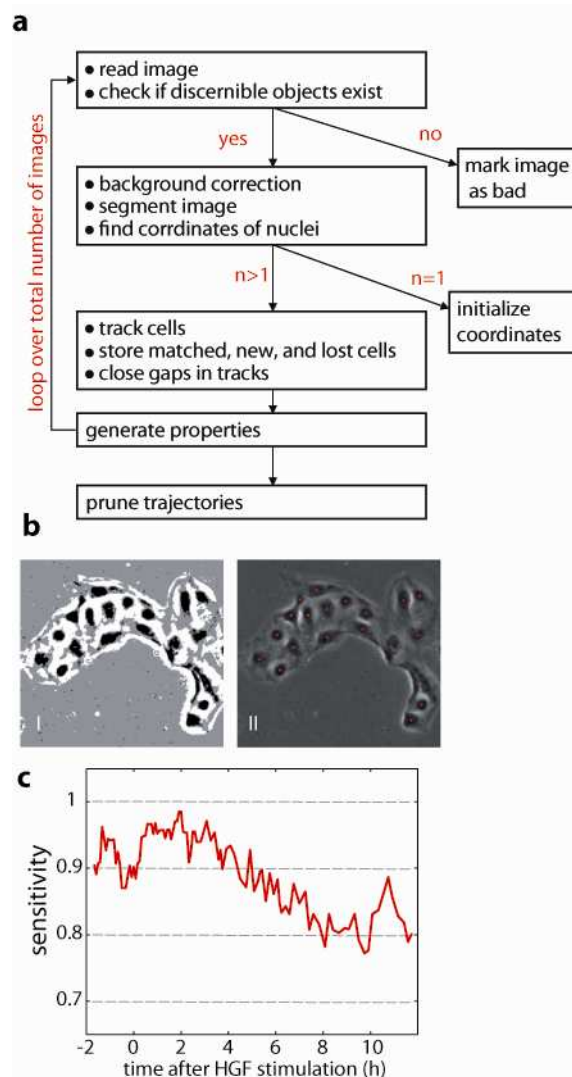


Figure S1. Cell tracking. **a** Schematic of the detection and tracking algorithm. **b** Segmented raw image (black: nuclear regions; white: cytoplasm; gray: background panel I) and extracted cell positions (red dots; panel II). **c** Sensitivity of automated detection: Ratio of automatically detected compared to manually detected cells over the course of a time lapse sequence double-tracked for the purpose of performance testing.

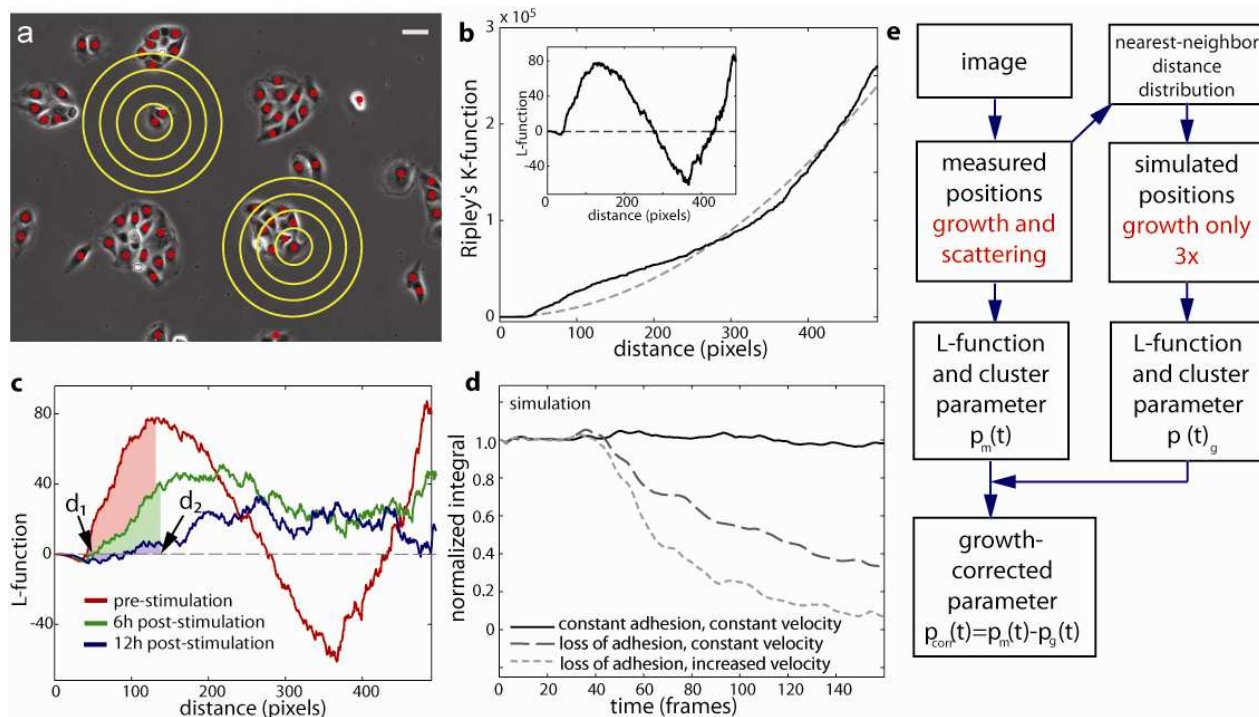


Figure S2. Definition of spatial dispersion parameter based on Ripley's K function. **a** Ripley's K-function measures the average number of neighbors within a circle of increasing radius r . Scale bar, 50 μm . **b** K-function and L-function (inset) for the distribution shown in a. **c** L-function at different time points before and after HGF-stimulation. d_1 is the distance at which the L-function prior to stimulation crosses zero (which corresponds to the average cell diameter); d_2 is the position of the first maximum of the L-function prior to stimulation (which corresponds to average cluster diameter). **d** Normalized partial integral of the L-function from d_1 to d_2 used to quantify spatial dispersal over time in simulated data sets of cell scattering. **e** Algorithm to compensate for distortion of the spatial dispersal parameter due to cell division.

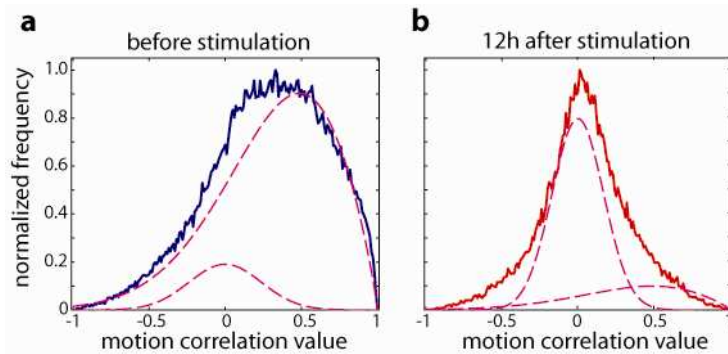


Figure S3. Definition of adhesion loss parameter based on motion correlation. **a** Histogram of correlation scores in a cell population before stimulation with HGF (n=358 cells measured for 20 frames). Fit of two superimposed distributions to determine the relative contributions of uncorrelated mode (Gaussian distribution with zero mean), or the subpopulation of detached cells; and correlated mode (positively skewed Weibull function), or the subpopulation of attached cells. **b** Histogram of correlation scores of cells between 10-12 hours after stimulation with HGF (n=792 cells measured for 20 frames).

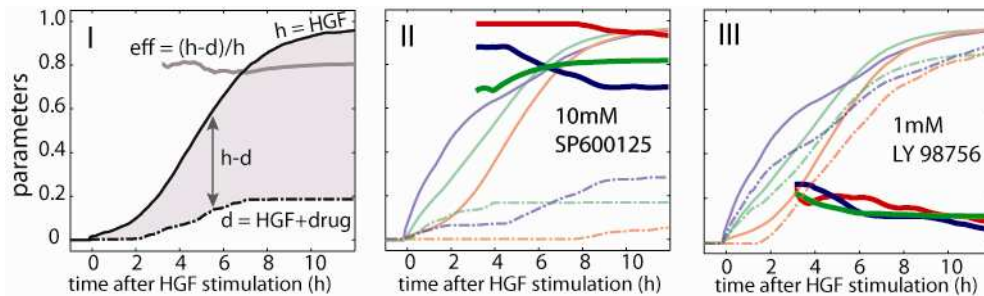


Figure S4. Inhibition efficiency for motility, dispersal, and adhesion loss parameters. Panel I: The inhibition efficiency of a drug ('HGF+drug') is calculated relative to a reference experiments with HGF stimulation only ('HGF'). Panels II and III: Parameter time courses (5 frame running average) for reference sample (dash-dotted lines) and drug-treated sample (solid lines) with calculated efficiency (bold lines; motility = red, adhesion loss = green, spatial dispersion = blue). Panel II displays a drug with strong inhibitory performance and panel III depicts a drug with weak inhibitory performance.

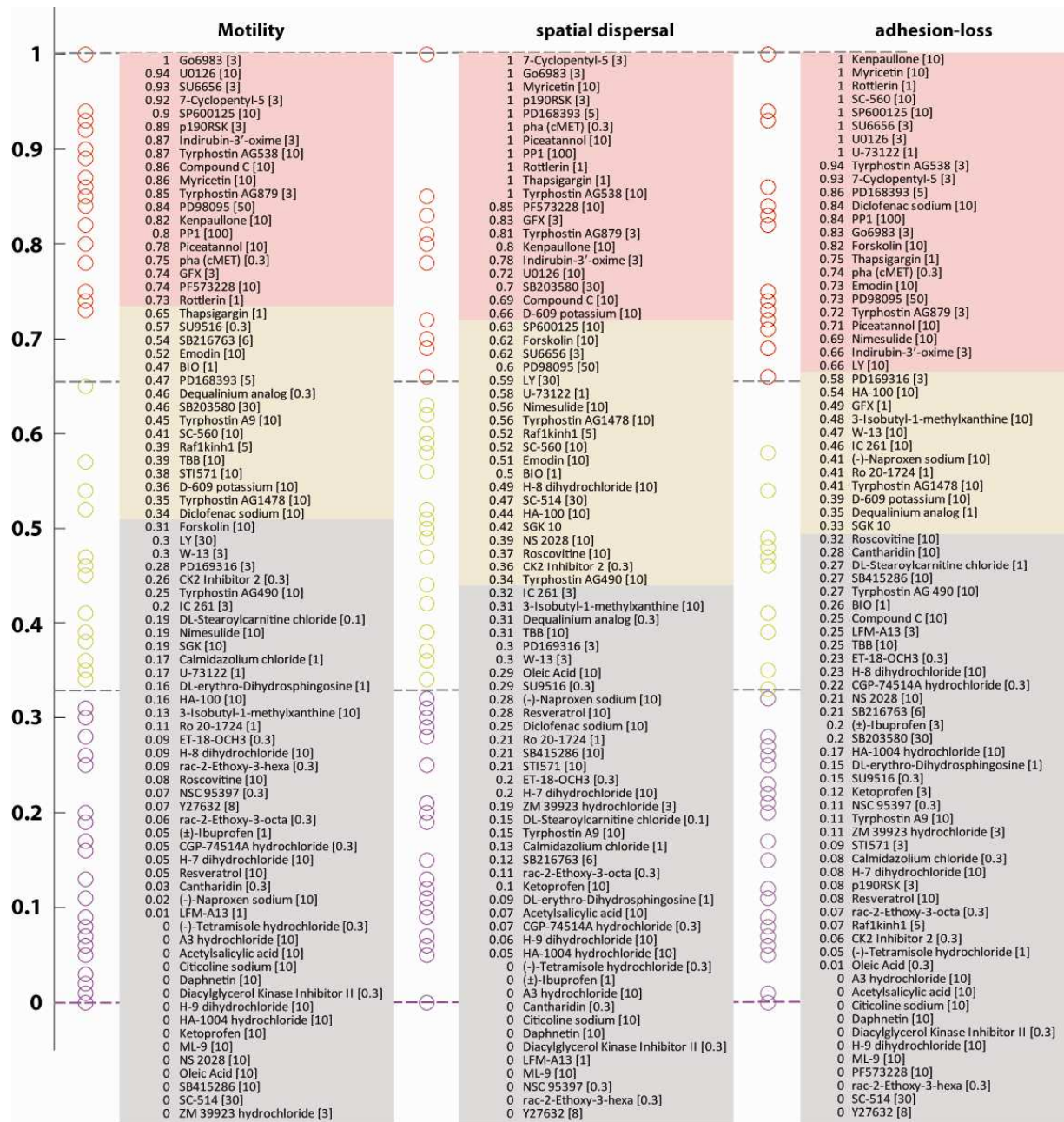


Figure S5. Ranked inhibition efficiencies. Inhibition efficiencies for motility increase, spatial dispersal, and adhesion loss of all screened drugs. Maximum efficiency is defined as the efficiency 12 hours post-stimulation (read out on the smoothed efficiency time course as shown in fig. Fig. S4). For graphical clarity, if multiple concentrations of a drug were used, only the efficiency of the most effective concentration is shown (concentration in square brackets in μM). Effective inhibitors were drugs with maximum efficiencies ranging from 67-100% (red); moderately effective inhibitors were drugs with maximum efficiencies ranging from 33-66% (yellow); ineffective inhibitors had maximum efficiencies below 33% (grey).

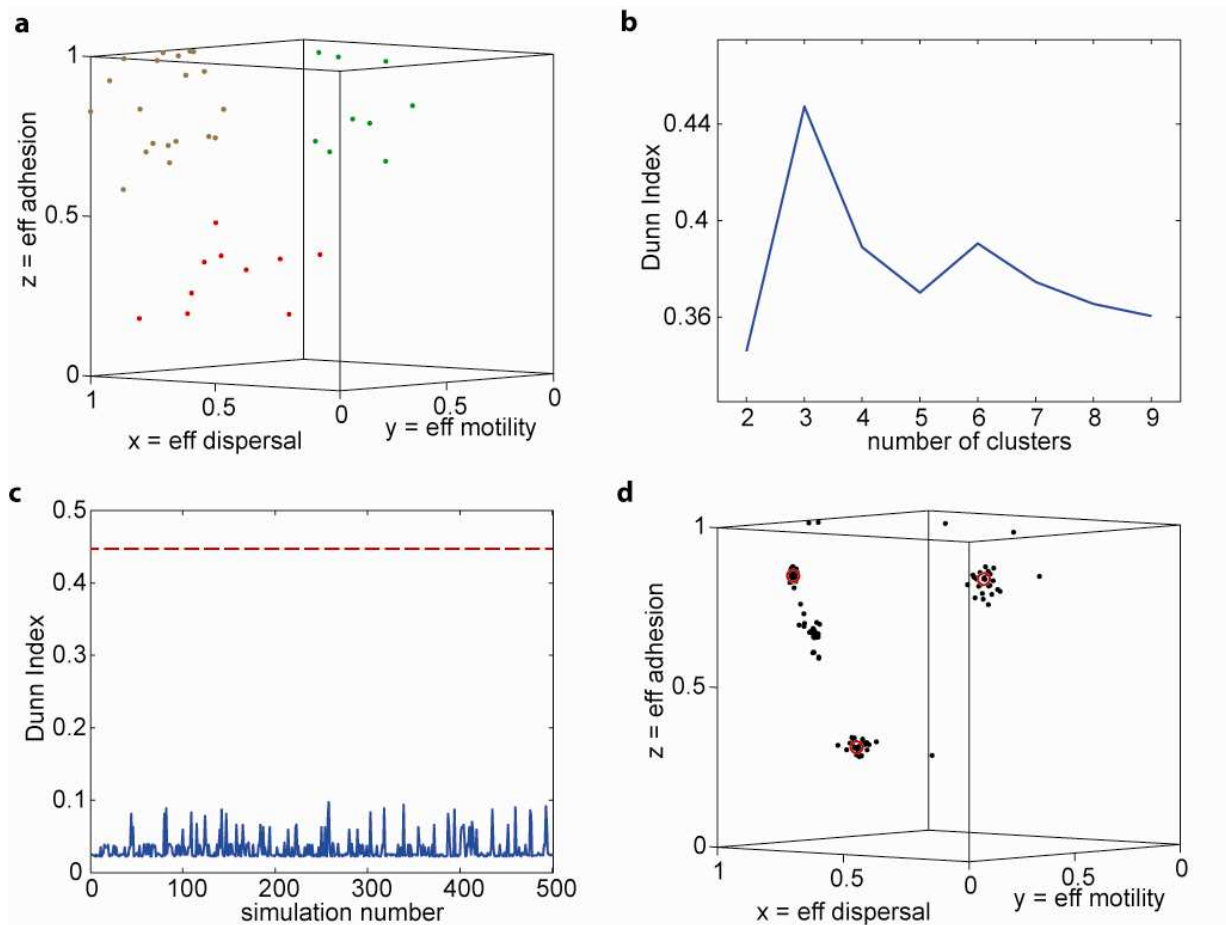


Figure S6. Validation of hierarchical clustering. **a** 3D scatter plot of the efficiencies of the drugs used for hierarchical clustering. Colors indicate the three identified clusters (green: adhesion-specific, red: motility-specific; brown: non-specific; see Fig. 5A). **b** The Dunn index for varying number of clusters. **c** The Dunn index for random assignment of data points to three clusters. Red dashed line indicates the Dunn index for the clusters selected in Fig. 5A. **d** 3D scatter plot of cluster centers for re-sampled data (black: re-sampled data sets; red: full dataset).

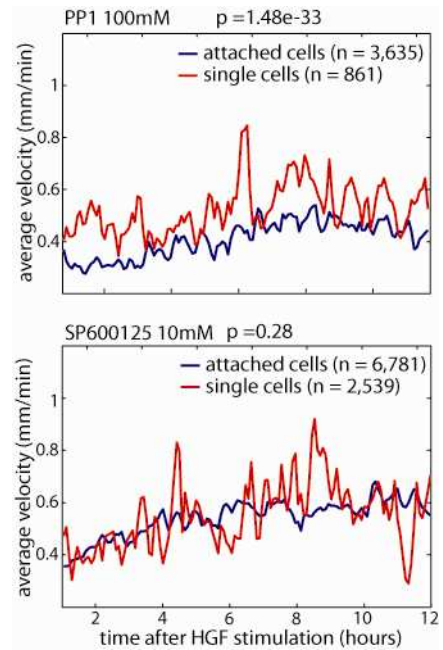


Figure S7. Velocity differences indicate adhesion specificity. Comparison of single-cell to clustered-cell velocities as an indicator for adhesion-specific effect of drugs. To test the significance of the velocity difference, a two-sided t-test was performed on the distributions of single-cell and clustered-cell velocities starting 1 hour after HGF stimulation. Upper panel: Example of high adhesion specificity (100 μ M PP1); significant difference between velocities. Lower panel: Example of efficient, yet non-specific drug (3 μ M Go6983); difference between velocities was not significant.

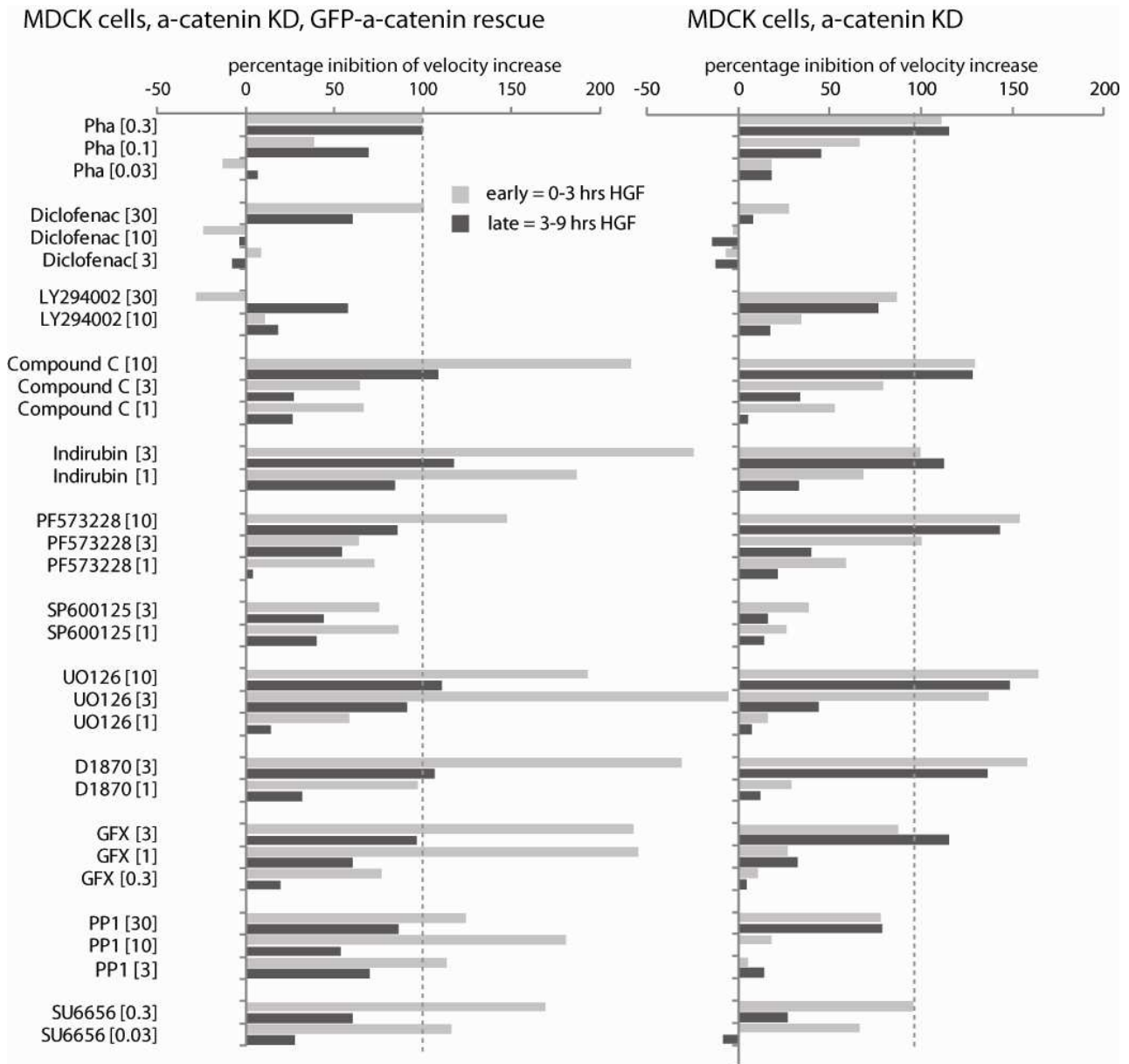


Figure S8: Inhibition efficiency of effective drugs on the scattering of normal and cell-cell junction-compromised MDCK cells. The average inhibition efficiency of the motility response in early (0-3 hours post HGF) and late phases (3-9 hours post HGF) of MDCK cell scattering is depicted for 12 efficient inhibitors, including the cMET inhibitor PHA-665752 as the positive control.

| molecular target(s) | Name | further information (if available) |
|---|------------------------------------|---|
| second messenger and lipid signaling | | |
| AC | Forskolin | Activates adenylate cyclase; |
| GC | NS 2028 | Specific soluble guanylyl cyclase inhibitor |
| PDE | Ro 20-1724 | Potent and selective cAMP phosphodiesterase inhibitor |
| PDE | 3-Isobutyl-1-methylxanthine | Potent phosphodiesterase inhibitor; more active than theophylline at adenosine receptors |
| PKA/PKG | H-9 dihydrochloride | Protein kinase inhibitor most effective for cAMP- and cGMP-dependent protein kinases |
| PKA/ PKG | H-8 dihydrochloride | |
| Ca ²⁺ | Thapsigargin | Potent, cell-permeable, IP ₃ -independent intracellular calcium releaser |
| Ca ²⁺ -ATPase | Calmidazolium chloride | Potent inhibitor of calmodulin activation of phosphodiesterase; strongly inhibits calmodulin-dependent Ca ²⁺ -ATPase |
| Calmodulin | W-13 | |
| COX | Acetylsalicylic acid | COX inhibitor; antithrombotic, COX-3 > COX-1 > COX-2 |
| COX | Diclofenac sodium | |
| COX | Ketoprofen | COX-1 selective non-steroidal anti-inflammatory (NSAID) drug |
| COX | (±)-Ibuprofen | non-selective COX inhibitor |
| COX | (-)-Naproxen sodium | COX-1 and COX-2 inhibitor |
| COX | Nimesulide | Highly selective COX-2 inhibitor |
| COX | SC-560 | Selective COX-1 inhibitor |
| COX | Resveratrol | Prevents apoptosis in K562 cells by inhibiting lipoxygenase and cyclooxygenase activity |
| DAGK | Diacylglycerol Kinase Inhibitor II | |
| PI3-kinase | LY294002 (LY) | |
| PKC / PLA2 / PLD | DL-erythro-Dihydrosphingosine | |
| PLA2 | Citicoline sodium | Phospholipase A2 inhibitor; neuroprotective in situations of hypoxia and ischemia |
| PLC, PLA2 | U-73122 | Phospholipase C and A2 inhibitor |
| PLD/PLC | D-609 potassium | inhibits phospholipase D and phosphatidylcholine phospholipase C (PIPLC) |
| PLC | ET-18-OCH ₃ | Phosphoinositide-specific Phospholipase C (PI-PLC) inhibitor |
| | | |
| protein kinases | | |
| cMET | PHA-665752 | c-MET inhibitor, serves as positive control |
| Abl | STI571 | |
| AMPK | Compound-C | selective AMPK inhibitor |
| BTK | LFM-A13 | |
| CDK | CGP-74514A hydrochloride | Cdk1 inhibitor |

| | | |
|------------------|--|--|
| CDK | Indirubin-3'-oxime | |
| CDK | Kenpaullone | Potent inhibitor of CDK1/cyclin B, CDK2/cyclin A, CDK2/cyclin E, and CDK5/p25 |
| CDK | SU 9516 | Cyclin-dependent kinase-2 (Cdk-2) inhibitor; induces apoptosis in colon cancer cells |
| CDK | Roscovitine | |
| CK | Myricetin | Casein Kinase II inhibitor |
| CK | TBB | Highly selective, ATP/GTP-competitive inhibitor of casein kinase 2 (CK2). |
| CK | IC 261 | Casein kinase-1 (CK-1delta/epsilon) inhibitor. |
| CK | A3 hydrochloride | Non-selective casein kinase (CK) inhibitor. |
| CK | CK2 Inhibitor 2 | High affinity, selective, ATP-competitive casein kinase 2 (CK2) inhibitor. |
| FAK | PF573228 | |
| GSK3 | SB216763 | |
| GSK3 | SB415286 | |
| GSK3 | BIO | ATP-competitive glycogen synthase kinase 3alpha/beta (GSK-3alpha/beta) inhibitor. |
| IKK | SC-514 | |
| JAK | Tyrphostin AG 490 | Jak-2 protein tyrosine kinase (PTK) inhibitor |
| JNK | ZM 39923 hydrochloride | Janus kinase 3 (JNK-3) inhibitor. |
| JNK | SP600125 | |
| MEK | U0126 | Specific inhibitor of MEK1 and MEK2 (MAP kinase kinase; MAPKK) |
| MEK | PD98059 | |
| MLCK | ML-9 | |
| MLCK | ML-7 | |
| p38 MAPK | PD 169316 | Potent, cell permeable and selective p38 MAP kinase inhibitor; nM potency |
| p38 MAPK | SB203580 | |
| p90 RSK | BI-D1870 | |
| PK | Daphnetin | |
| PK | HA-1004 hydrochloride | Potent inhibitor of cAMP- and cGMP-dependent protein kinases; because it has low affinity for protein kinase C, HA-1004 serves as an excellent negative control of H-7 HCl |
| PKA / PKC | H-7 dihydrochloride | |
| PKA / PKC / MLCK | HA-100 | |
| PKC | Dequalinium analog, C-14 linker | Protein kinase C-alpha (PKC-alpha) inhibitor |
| PKC | rac-2-Ethoxy-3-octadecanamido-1-propylphosphocholine | |
| PKC | rac-2-Ethoxy-3-hexadecanamido-1-propylphosphocholine | |
| PKC | Oleic Acid | Activates protein kinase C in hepatocytes; uncouples oxidative phosphorylation |
| PKC | DL-Stearoylcarnitine chloride | |
| PKC | GF109203X (GFX) | similarly high affinities for PKC a, b, g, d, e |

| | | |
|-----------------------------|--|---|
| PKC | Go6983 | similarly high affinities for PKC a, b, g, d |
| PKC / CaM Kinase III | Rottlerin | PKCd selective and CaM kinase III inhibitor |
| Raf | Raf1Kinh1 | |
| ROCK | Y-27632 | Rho-associated coiled-coil forming protein kinase (ROCK) inhibitor. Also inhibits ROCK-II. |
| RTK | Tyrphostin AG 1478 | EGFR |
| RTK | PD168393 | EGFR |
| RTK | Tyrphostin AG 538 | IGF-1 R |
| RTK | Tyrphostin A9 | PDGFR |
| RTK | Tyrphostin AG 879 | Tyrosine kinase nerve growth factor receptor (TrkA) inhibitor; inhibits 140 trk protooncogene and HER-2 |
| Src | 7-Cyclopentyl-5-(4-phenoxy)phenyl-7H-pyrrolo[2,3-d]pyrimidin-4-ylamine | Potent and selective Lck (src family tyrosine kinase) inhibitor. |
| Src | Emodin | p56lck Tyrosine kinase inhibitor |
| Src | Piceatannol | Non-receptor kinase Syk and Lck inhibitor |
| Src | PP1 | high affinity for Lck and Fyn, lower for Src |
| Src | SU6656 | high affinity for Src, Fyn, Yes, Lyn. Lower affinity for Lck |
| | | |
| protein phosphatases | | |
| PP2A | Cantharidin | Protein phosphatase 2A inhibitor |
| Cdc25 | NSC 95397 | Selective, irreversible Cdc25 dual specificity phosphatase inhibitor. |
| AP | (-)-Tetramisole hydrochloride | Inhibits multiple mammalian alkaline phosphatases |

Table S1: Target names and additional information on drugs used in screen.

References

1. Ponti, A., A. Matov, M. Adams, S. Gupton, C. M. Waterman-Storer, and G. Danuser. 2005. Periodic patterns of actin turnover in lamellipodia and lamellae of migrating epithelial cells analyzed by quantitative Fluorescent Speckle Microscopy. *Biophys J* 89: 3456-3469.
2. MacQueen, J. 1967. Some methods for classification and analysis of multivariate observations. *Proceedings of 5-th Berkeley Symposium on Mathematical Statistics and Probability* 281-297.
3. Jaqaman, K., D. Loerke, M. Mettlen, H. Kuwata, S. Grinstein, S. L. Schmid, and G. Danuser. 2008. Robust single-particle tracking in live-cell time-lapse sequences. *Nat Methods* 5: 695-702.
4. Dunn, G. A., and A. F. Brown. 1987. A unified approach to analysing cell motility. *Journal of cell science. Supplement* 8: 81-102.
5. DiMilla, P. A., J. A. Quinn, S. M. Albelda, and D. A. Lauffenburger. 1992. Measurement of individual cell migration parameters for human tissue cells. *AIChE Journal* 38: 1092-1104.
6. Ripley, B. D. 1976. 2nd-Order Analysis of Stationary Point Processes. *Journal of Applied Probability* 13: 255-266.
7. Mattfeldt, T. 2005. Explorative statistical analysis of planar point processes in microscopy. *J Microsc* 220: 131-139.
8. Reilly, C., Schacker, T., Haase, A. T., Wietgreffe, S., Krason, D. 2002. The clustering of infected SIV cells in lymphatic tissue. *J. A. Sat. Ass.* 97: 943-954.
9. Beil, M., F. Fleischer, S. Paschke, and V. Schmidt. 2005. Statistical analysis of the three-dimensional structure of centromeric heterochromatin in interphase nuclei. *J Microsc* 217: 60-68.
10. Ehrlich, M., W. Boll, A. Van Oijen, R. Hariharan, K. Chandran, M. L. Nibert, and T. Kirchhausen. 2004. Endocytosis by random initiation and stabilization of clathrin-coated pits. *Cell* 118: 591-605.
11. Hess, S. T., M. Kumar, A. Verma, J. Farrington, A. Kenworthy, and J. Zimmerberg. 2005. Quantitative electron microscopy and fluorescence spectroscopy of the membrane distribution of influenza hemagglutinin. *J Cell Biol* 169: 965-976.
12. Philimonenko, A. A., J. Janacek, and P. Hozak. 2000. Statistical evaluation of colocalization patterns in immunogold labeling experiments. *J Struct Biol* 132: 201-210.
13. Prior, I. A., C. Muncke, R. G. Parton, and J. F. Hancock. 2003. Direct visualization of Ras proteins in spatially distinct cell surface microdomains. *J Cell Biol* 160: 165-170.

14. van Rheenen, J., E. M. Achame, H. Janssen, J. Calafat, and K. Jalink. 2005. PIP2 signaling in lipid domains: a critical re-evaluation. *EMBO J* 24: 1664-1673.
15. Haase, P. 1995. Spatial pattern analysis in ecology based on. Ripley's K-function: Introduction and methods of edge correction. *J. Veg. Science* 6: 575-582.
16. Handl, J., J. Knowles, and D. B. Kell. 2005. Computational cluster validation in post-genomic data analysis. *Bioinformatics* 21: 3201-3212.
17. Dunn, J. C. 1974. Well separated clusters and optimal fuzzy-partitions. *Journal of Cybernetics* 4: 95-104.

Movie S1. The presence of cell-cell adhesions slows down HGF-induced cell motility.

Time lapse image series of MDCK cell behavior under indicated conditions. Left panel – unstimulated cells; middle panel – HGF-stimulated cells; right panel – HGF-stimulated cells in low $[Ca^{2+}]$ condition. Color-coded tails ('dragtails') indicate the automatically determined cell-positions in the previous 6 frames. Thus, the length of the dragtail is indicative of the instantaneous velocity. 5 ng/ml HGF was added to the indicated samples 115 min after the start of imaging (frame 19). Frame rate: 6 min.

Movie S2. Motility Parameter

Left panel: Phase-contrast image of cell distribution with detected cell positions as colored dots; scale bar 50 μm , frame rate 5 min. Middle panel: Normalized histogram of measured current average cell velocities, triangle denotes position of the mean. Right panel: Time course of normalized average velocity.

Movie S3. Spatial Dispersion Parameter

Left panel: Phase-contrast image of cell distribution with detected cell positions as colored dots; scale bar 50 μm , frame rate 5 min. Middle panel: L-function of measured current cell distribution; shaded area denotes the distances over which the partial integral is performed. Right panel: Time course of normalized partial integral.

Movie S4. Adhesion Loss Parameter

Left panel: Phase-contrast image of cell distribution with detected cell positions as colored dots; scale bar 50 μm , frame rate 5 min. Middle panel: Normalized histogram of correlation values in the current frame; red and magenta curves indicate the fitted attached (zero-mean) and detached (positive-mean) distributions. Right panel: Time course of the normalized ratio of the respective areas of the fitted attached or detached distributions.

Movie S5. α -Catenin–depleted cells do not form functional cell-cell junctions

Time lapse image series of HGF-induced scattering in MDCK cells stably expressing an α -catenin targeting shRNA. In the left panel, cell-cell junction formation was rescued in these cells by overexpression of GFP- α -catenin. 5 ng/ml HGF was added to the indicated samples 2 hours after the start of imaging (frame 20). Frame rate: 6 min.

Movie S6. Knockdown of CDK1 but not CDK5 inhibits the HGF-induced increase in cell motility.

Representative areas from time lapse image series of cell scattering in response to HGF of DU145 cells transfected with siRNAs directed against cMET, CDK1, or CDK5 as indicated. 5 ng/ml HGF was added 2 hours after the start of imaging (frame 20). Frame rate: 6 min.

Movie S7. Diclofenac inhibits the HGF-induced loss of cell-cell adhesion, whereas knockdown of COX-2 reduces the stability of cell-cell junctions.

Representative areas from time lapse image series of HGF-induced cell scattering of MDCK cells transfected with scrambled (non-targeting) or COX-2-targeting shRNA compared to untransfected MDCK cells treated with 10 μ M diclofenac just prior to the start of imaging. 5 ng/ml HGF was added 1.5 hours after the start of imaging (frame 15). Frame rate: 6 min.

Movie S8. Blocking RSKs by chemical inhibition or by siRNA-mediated knockdown inhibits the HGF-induced increase in cell motility.

Representative areas from timelapse image series of HGF-induced cell scattering of untransfected DU145 cells in the absence or presence of 3 μ M BI-D1870 (added just prior to the start of imaging) and DU145 cells transfected with scrambled or RSK1- and RSK2-targeting siRNAs. 5 ng/ml HGF was added 2 hours after the start of imaging (frame 20). Frame rate: 6 min.